**Journal of Cleaner Production**

Volume 203, 1 December 2018, Pages 418-426

# Hydrogen production from industrial wastewaters: an integrated reverse electrodialysis - water electrolysis energy system[1]

Ramato Ashu Tufa[a,*], Jaromir Hnát [a], Michal Němeček [a], Roman Kodým [a], Efrem Curcio[b,c], and Karel Bouzek[a]

[a] *Department of Inorganic Technology, University of Chemistry and Technology Prague, Technická 5, 166 28 Prague 6, Czech Republic*

[b] *Department of Environmental and Chemical Engineering, University of Calabria (DIATIC-UNICAL) via P. Bucci CUBO 45A, 87036 Rende (CS) Italy*

[c] *Institute on Membrane Technology of the National Research Council (ITM-CNR), c/o the University of Calabria, via P. Bucci, cubo 17/C, 87036 Rende, CS, Italy*

[1]DOI: 10.1016/j.jclepro.2018.08.269

## Abstract

This work presents a novel approach combining reverse electrodialysis (RED) and alkaline polymer electrolyte water electrolysis (APWEL) for renewable hydrogen production. APWEL is fuelled by salinity gradient power (SGP) extracted from sulfate ($SO_4^{2-}$)-rich industrial wastewater. The performance of a pilot-scale RED unit (200 cells, active area: 31.5×63.5 $cm^2$), using salt solutions mimicking sulfate-rich waste streams (0.01-0.3 M $Na_2SO_4$), was evaluated. An open circuit voltage (OCV) of 12.3 V, a maximum power density of 0.22 $W/m^2MP$ (MP: membrane pair) and internal area resistance of 43.2 $\Omega cm^2$/cell were recorded by using 0.01 M/0.3 M $Na_2SO_4$ solutions at 35 $^oC$. The APWEL stack (6 cells, active area: 5×5 $cm^2$), equipped with Ni foam electrodes and heterogeneous anion-selective membranes, was tested with varying concentrations of liquid electrolyte (0.85-2.5 M KOH) and varying temperatures (28-48 $^oC$). The APWEL stack attained a maximum current density of 110 $mA/m^2$ at 1.85 V/cell (i.e. 11 V per stack), 2.5 M KOH and 48$^oC$. Under these conditions, the integrated system exhibited a maximum hydrogen production rate of 50 $cm^3/h \cdot cm^2$. This study opens up a new perspective on renewable hydrogen production fuelled by non-intermittent SGP from $SO_4^{2-}$-rich industrial effluents.



**Keywords:** Industrial wastewater, reverse electrodialysis, salinity gradient power, water electrolysis, hydrogen production

## 1. Introduction

Hydrogen is a clean and versatile energy carrier for the future. It can be produced from water, natural gas, biomass and various other sources. Over the last decade, hydrogen production using water electrolysis has found acceptability due to the simplicity of this technology and the possibility to produce hydrogen of high purity. Moreover, water electrolysis is a flexible process driven by renewable energy resources, such as solar and wind power. More recently, the use of salinity gradient power (SGP) generated by reverse electrodialysis (RED) as a non-intermittent power source to fuel water electrolyzers has also been explored as an interesting alternative for renewable hydrogen production (Tufa et al., 2017; Tufa et al., 2016). In RED, cation-exchange membranes (CEMs) and anion-exchange membranes (AEMs) are alternately aligned to create a low-concentration compartment (LCC) and a high-concentration compartment (HCC) which are fed with solutions of low and high concentrations, respectively. A scheme of RED is shown in Figure 1. The transport of ions occurs through ion-exchange membranes from HCC to LCC solutions driven by the electrochemical potential difference. Electricity is generated by a redox reaction evolving over electrodes placed at the ends of the membrane pile. RED technology is mostly investigated at lab-scale (Farrell et al., 2017), while studies of large-scale RED systems for SGP generation are relatively rare. A more recent demonstration of a pilot-scale RED system involved the testing of a stack equipped with 125 cell pairs (44×44 $cm^2$) and using brine and brackish water from salt works (Tedesco et al., 2016).

Alkaline water electrolysis represents a mature process for hydrogen production combining the advantages of robustness and relatively low capital and operating costs. However, it has several limitations, such as inadequately optimized separator, low process efficiency and lack of suitability for intermittent power operations (Chanda et al., 2015). The latest development in alkaline water electrolysis is alkaline polymer electrolyte water electrolysis (APWEL), which employs a solid polymer electrolyte based on AEMs (Hnát et al., 2011; Xiao et al., 2012). Such a design has the advantage of low gas cross-over, higher flexibility, and suitability for scale-up and operability at high pressure, allowing a simplified system with lower costs. In fact, most APWEL studies focus on single-cell designs rather than multiple-cell designs; the latter allow a better understanding of system performance on a large scale. Therefore, the present

study uses scaled-up RED and APWEL systems in contrast to the set-ups used in most of the previous studies.

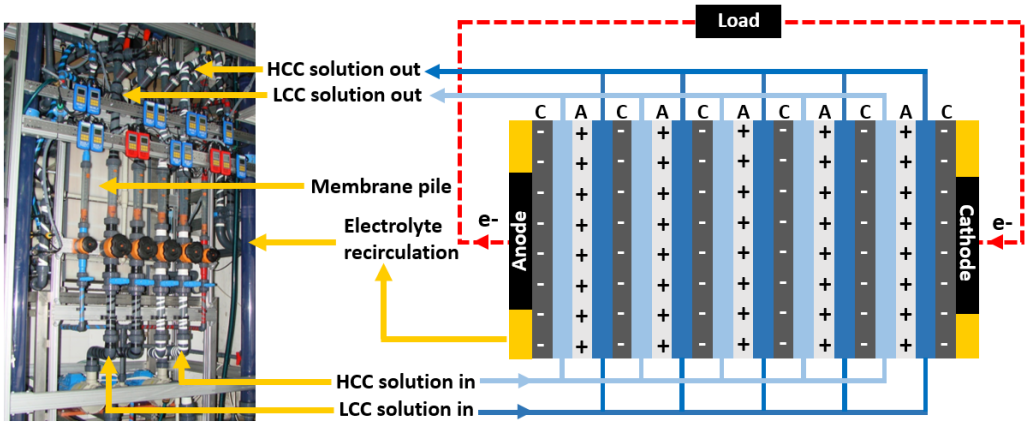


**Figure 1.** Picture and scheme of the pilot-scale RED set-up (HCC: high-concentration compartment; LCC: low-concentration compartment. C: Cation-exchange membrane, A: Anion-exchange membrane.

Industrial waste streams discharged into the ocean have SGP potential of up to 18 GW (Logan and Elimelech, 2012). However, the performance of RED using waste streams from various sources (Dil et al., 2017a; Dil et al., 2017b; Luo et al., 2017; Mehrabi and Alipanahpour Dil, 2017) other than NaCl-based salt solutions is a poorly investigated topic. Recent attempts have focused on the application of hybrid RED/electrodialysis systems for power generation using phenol-containing wastewaters (Luo et al., 2017), and wastewater from a fish canning factory and a sewage treatment plant (Di Salvo et al., 2017). Meanwhile, hydrogen production from waste resources is a rapidly growing field. In particular, biological hydrogen production from industrial wastewaters containing organic matter is regarded as a promising strategy for renewable hydrogen production; however, the drawback of this process is the low yield (Hatzell et al., 2014). On the other hand, given an electrolyzer's energy consumption of 53-70 kWh/kg (Levene et al., 2007), efficient exploitation of SGP produced from waste streams to fuel water electrolyzers would produce an annual yield of up to 3 M tons of hydrogen. Therefore, indirect production of hydrogen from industrial waste streams by water electrolyzers may be a viable alternative to other renewable hydrogen technologies.

Most industrial waste streams are rich in $SO_4^{2-}$ which can be converted into renewable energy and hydrogen. $SO_4^{2-}$-rich waste streams are usually obtained from salt lake brines, mining processes and industrial waste streams from sewage treatment plants, tanneries and rechargeable battery manufacturing processes. In most cases, industrial wastewaters contain sulfate concentrations from 1-40 g/L (0.01-0.4 M ) (Siles et al., 2010), which is far above the permitted limit (0.75-1.5 g/L) of discharge to surface water bodies (Act, 2003). A high content of $SO_4^{2-}$ brine with concentrations of up to ~1 M can be obtained from membrane treatment of industrial wastewater (Quist-Jensen et al., 2017). Therefore, $SO_4^{2-}$-rich industrial wastewaters can potentially be exploited for SGP generation and subsequent hydrogen production in the logic of the circular economy, waste-to-energy (WtE) and power-to-gas (P2G) (Götz et al., 2016).

To our knowledge, no attempt has been made to produce SGP from $SO_4^{2-}$-rich industrial effluents with subsequent use as fuel for hydrogen production by water electrolysis. In the present study, a novel approach is investigated, combining SGP RED and APWEL systems for hydrogen production driven by non-intermittent energy generated from $SO_4^{2-}$-rich industrial waste streams. The process is conceptually illustrated in Figure 2. Two key objectives were set. Firstly, a pilot-scale RED unit was optimized for SGP generation using industrial waste streams: the performance of the RED unit was evaluated in terms of voltage and power density at varying flow velocity and temperature of waste streams. Next, a laboratory-scale APWEL system, scaled-up 6-fold compared to most cases studied using single-cell designs (Ju et al., 2018; Tufa et al., 2016), was tested for potential hydrogen production driven by SGP: the hydrogen production rate was evaluated at varying electrolyte concentrations and temperatures to identify optimal operating conditions. The ultimate goal was to demonstrate the possibility of converting the electrochemical potential of industrial waste streams into clean energy and hydrogen by an integrated RED-APWEL energy system.

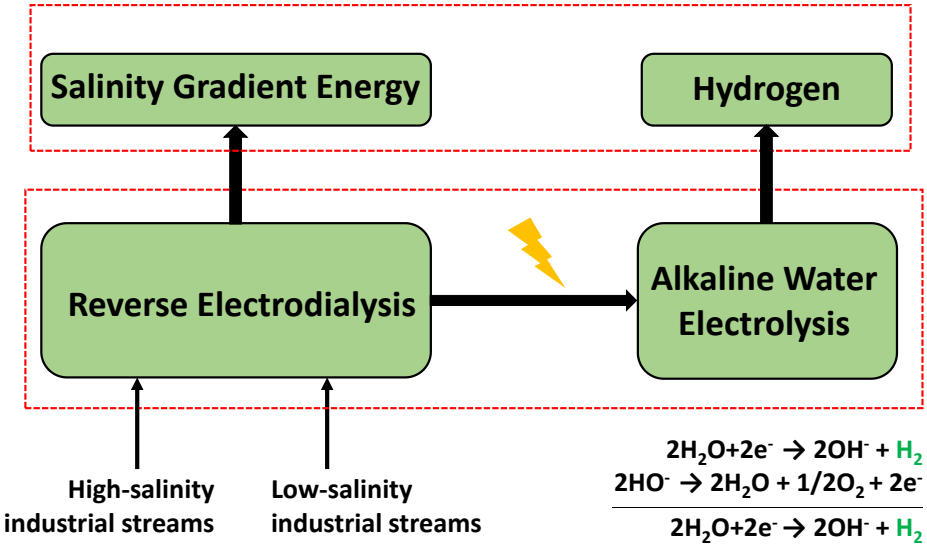


**Figure 2.** Conceptual illustration of renewable hydrogen production by an integrated reverse electrodialysis and alkaline polymer electrolyte water electrolysis energy system.

## 2. Materials and methods

### *2.1. Pilot-scale reverse electrodialysis stack*

A commercial pilot-scale EDR-III/500/0.8 unit (MEGA a.s., Czech Republic) was adapted to a RED configuration in co-flow mode. A picture of the pilot-scale RED used in the present study is shown in Figure 1. The stack consisted of 200 cell pairs with alternatively aligned ion-exchange membranes, each separated by non-woven, net-like spacers made of polyethylene having a porosity of 0.88 and thickness of 0.8 mm. These spacers have openings in their frameworks, resulting in horizontal feed and drain channels in the membrane stack. The electrodes used were made of platinized titanium (Ti/Pt) and had the same effective area as the membranes. Aqueous solutions of $Na_2SO_4$ were used as test solutions in all experiments. An electrode rinse solution of 0.5 M $Na_2SO_4$ (99.0 %, Penta s.r.o., Czech Republic) was used to sustain the redox reaction for the continuous flow of electricity through the external load. The use of $Na_2SO_4$ is environmentally safer in large-scale RED operations (Tufa, 2015; Veerman et al., 2010b).

105 *2.1.1. Membranes*

106 Ralex ion-exchange membranes (MEGA a.s., Czech Republic) with a thickness
107 of 0.57 mm, an effective area 2000 $cm^2$ (31.5 cm x 63.5 cm) and total active membrane
108 area of 80 $m^2$ were used in the pilot-scale RED unit. These membranes have higher ion-
109 exchange capacity compared to most commercial membranes, along with a reasonable
110 permselectivity i.e. capability to permit counter-ions while excluding co-ions. The
111 electrochemical properties of Ralex membranes are shown in Table 1.

112 *2.1.2. Feed solutions*

113 Aqueous solutions of $Na_2SO_4$ were used as test solutions in all experiments. The
114 LCC solution had a concentration of 0.01 M $Na_2SO_4$, the HCC solution a concentration
115 of 0.3 M $Na_2SO_4$. The concentration of feed solutions was monitored at regular time
116 intervals by conductivity measurement (GREISINGER GMH 3430, Czech Republic).
117 Experiments were performed in batch mode by recirculation of feed solutions at a flow
118 rate in the range of 1-11 $m^3/h$ (flow meter GEORG FISHER+GF+, USA) and
119 temperature in the range of 15 - 35°C.
120
121 Table 1. Properties of the ion-exchange membranes used in the present study (Güler et
122 al., 2013).
123

| **Membrane** | **Thickness** (μm) | **Areal resistance** ($\Omega cm^2$) | **Permselectivity** (%) | **Ion-exchange capacity** (meq./g) | **Charge density** (meq./g $H_2O$) |
|---|---|---|---|---|---|
| Ralex AMH-PES | 714 | 7.66 | 89.3 | 1.97 | 3.5 |
| Ralex CMH-PES | 764 | 11.3 | 94.7 | 2.34 | 7.6 |

124

125 *2.1.3. Electrochemical measurements.*

126 An external precision resistor (Fuel Cell test load, TL4A, Astris Energi Inc., USA),
127 connected in series with the RED system, was used for loading the stack (Tufa et al.,
128 2014). The DC current and voltage levels across the test loads were measured by a Fluke
129 87-V Digital Multimeter (USA). A response time of about 30 minutes was maintained
130 between each experimental run for $Na_2SO_4$ feed solutions to achieve a stable voltage.
131 The overall performance of the RED stack was evaluated in terms of voltage ($V$), current

($I$) and gross power density ($P_d$). Theoretical approaches to an evaluation of the performance of the RED stack are provided in the Supporting Information.

### *2.2. Alkaline water electrolysis stack*

#### *2.2.1. Design and assembly of the membrane electrode*

The APWEL unit, in a bipolar configuration, was equipped with 6 cells, each having an active area of 5×5 $cm^2$. A picture and scheme of the APWEL unit is presented in Figure 3. The anodes and cathodes were based on porous Ni foam (INCO Advanced Technology Materials Co, Ltd., USA) with a thickness of 1.7 mm and a pore size of 0.58 mm. The end plates of the APWEL stack were made of steel, the insulating plates of PVC (polyvinyl chloride) (PLEXIPLAST, Czech Republic). Nickel sheets (KÖNIG FRANKSTAHL s.r.o., Czech Republic) were used as current collectors and bipolar plates. Distribution plates, serving both for the housing of the Ni foam electrodes and the distribution of the liquid electrolyte, were made of polyethylene (PE) (TITAN-MULTIPLAST s.r.o., Czech Republic). Expanded polytetrafluoroethylene sealing was used to prevent leakage of the electrolyte from the stack. The flow of the liquid electrolyte was 4.6 $cm^3/s$ throughout the stack. The separators of the gases produced were made of polymethyl methacrylate (Zenit, spol. s.r.o., Czech Republic) and filled with polyethylene rollers in order to increase the linearity of the flow and interfacial contact, and thus the separation rate of the gaseous phase.

The heterogeneous membranes produced in-house were composed of an inert matrix of low-density polyethylene (LDPE 605 BA, ExxonMobil TM, LD 605BA, USA) (27.3 wt.%) and a water-soluble component of poly(ethylene glycol-*ran*-propylene glycol) (6.7 wt.%) (Sigma-Aldrich, USA) blended with anion-selective resins (Dowex Marathon, USA) with quaternary ammonium functional groups. Details of the preparation, characterization and activation methods of the anion-selective membrane (ASM) are given elsewhere (Hnát et al., 2012). For the present study, the membranes were reinforced with polyethylene terephthalate to improve the mechanical properties. The properties of the ASMs are presented in Table 2.

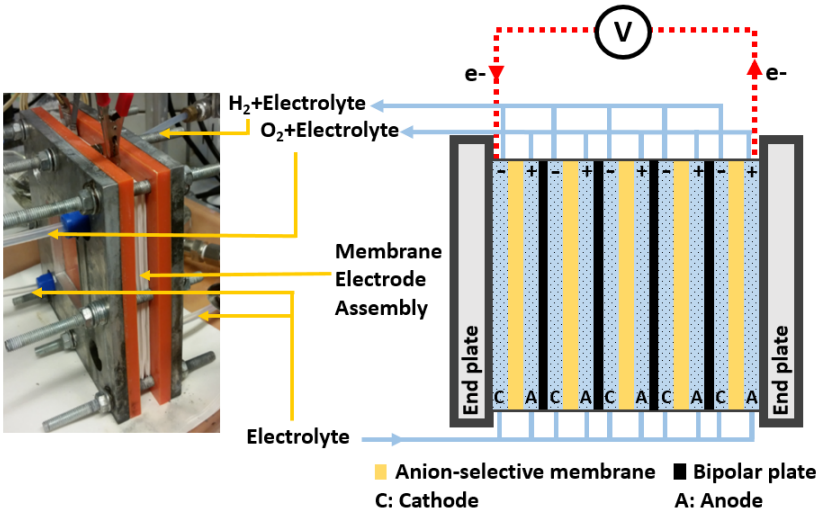


**Figure 3.** Picture and scheme of the lab-scale electrolyzer with zero-gap membrane electrode assembly.

*2.2.1. Electrochemical measurements.*

The voltage of the APWEL stack was recorded for an input current range of 0.25 A - 9.75 A (corresponding to current densities in the range of 0.01-0.39 A/cm$^2$) supplied by a DC power source Statron 3251.1 (Statron Gerätetechnik GmbH, Germany). The current-voltage curve was recorded at KOH (85.0 %, Penta s.r.o., Czech Republic) concentration in the range of 0.85-2.5 mol/dm$^3$ and temperature in the range of 28-48 $^{o}$C. The hydrogen production rate (*HPR*) under different conditions can be determined from $I_e$ flowing through the APWEL.

The minimum amount of energy required to initiate the water electrolysis reaction is $\Delta G$ = 237.2 kJ/mol, corresponding to the reversible voltage of $V_R$ =1.23 V. However, under practical conditions the cell voltage ($V_{cell}$) is given by:

$$V_{cell} = V_R + \eta_{act} + I_e R_{Ohm} \quad (1)$$

where $\eta_{act}$ is the activation overpotential of electrode reactions, $I_e$ the cell current and $R_{Ohm}$ the Ohmic resistance associated with electrolyte properties, electrode type and cell design. The thermoneutral voltage ($V_{th}$) corresponds to the condition where the energy dissipated by electric current is used to overcome $\Delta G$ for the splitting of water molecules which is related to the redox processes as well as the change in entropy ΔS. $V_{th}$ is related to the change in enthalpy ΔH as:

$$V_{th} = \frac{\Delta H}{nF} \quad (2)$$

where $n$ is the number of electrons involved in the redox reaction and $F$ is the faraday constant (96,485 C/mol). $V_{th}$ is equal to 1.48 V at 25 °C. Industrial-scale alkaline electrolyzers operate at a cell voltage of 1.8-2.0 V and a current density of 100-300 mA/cm$^2$ (Wang et al., 2014; Zeng, K. and Zhang, D.K., 2010). The power dissipated over the electrolyzer ($P_e$) can be obtained from the cell voltage and cell current:

$$P_e = V_{cell} I_e \tag{3}$$

The energy consumed by the electrolyzer $W_e$ (kWh/Nm$^3$) with 100 % Faradaic efficiency is given by:

$$W_e = V_{cell} nF \tag{4}$$

The energy requirements of industrial-scale alkaline electrolyzers usually amount to 4.5-5.0 kWh/Nm$^3$ (Wang et al., 2014; Zeng, K. and Zhang, D.K., 2010), the theoretical value is 2.9 kWh/Nm$^3$, thus implying a thermodynamic efficiency of about 58-64% (Wang et al., 2014). The hydrogen production rate (*HPR*) can be determined from $I_e$ as:

$$HPR = \frac{I_e}{nF} \eta_e \tag{5}$$

where $\eta_e$ is the conversion efficiency (current efficiency) factor depending on gas losses due to parasitic currents and hydrogen permeation into the anode compartments. $\eta_e$ can be determined from the theoretical hydrogen production rate $HPR_t$ as:

$$\eta_e = \frac{HPR}{HPR_t} x100 \tag{6}$$

Table 2. Properties of the heterogeneous ASM used in an APWEL unit (Hnát et al., 2012; Tufa et al., 2016).

| Membrane Properties | Temperature (°C) | Values determined |
|---|---|---|
| Thickness (mm) | 20 | 0.74 |
| Ion-exchange capacity (mmol/g dry) | 20 | 2 |
| | 30 | 3.8 |
| Conductivity (S/m) | 50 | 5.1 |

## 3. Results and discussion

### *3.1. Power generation in pilot-scale reverse electrodialysis*

The dependence of power generated by RED on temperature (15-35ºC) and flow velocity (0.6-6.9 cm/s) was evaluated in order to identify conditions for the highest power output. The RED stack was operated with 0.01M/0.3 M $Na_2SO_4$ feed solutions.

### *3.2. Effect of flow velocity and temperature*

#### *3.2.1.* OCV of the stack

An increase in flow velocity improves the hydrodynamic mixing and hence facilitates the mass transfer of ions towards the membrane surface. Moreover, the flow velocity is directly related to the residence time of the solution in the RED stack. If the flow velocity is increased by two-fold, the residence time is reduced by half. Thus, it has a direct impact on the salinity gradient distribution across the channels of the stack.

Figure 4 presents the polarization curves as a function of flow velocity and temperature. An increase in OCV of up to 9.7% - from 10.9V to 12V - was observed on raising the flow velocity from 0.6 to 6.9 cm/s (Figure 4a). A viable explanation is a change in the local salinity gradient due to the flowing parasitic current. In fact, a much higher impact of flow velocity on OCV was observed in previous studies on small-scale RED designs (Tufa et al., 2015); this was ascribed to the higher salinity gradient and thinner membranes used in such cases which promote concentration changes caused by the parasitic current.

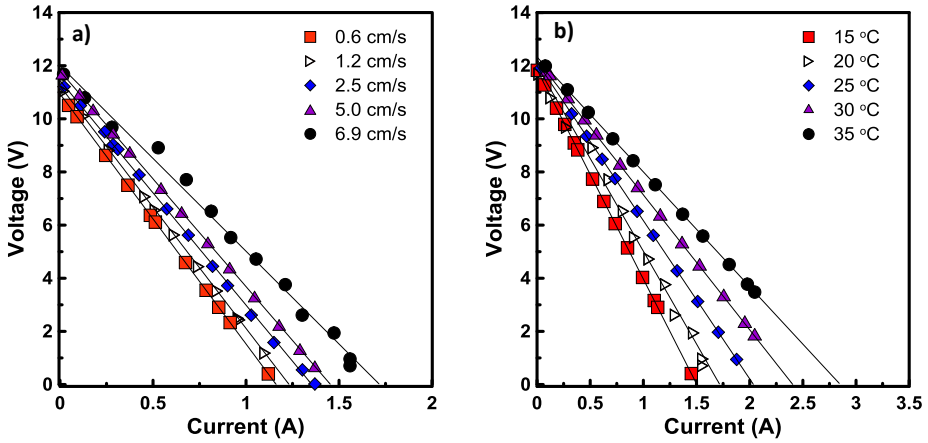


**Figure 4.** RED polarization (I-V) curves: a) at different flow velocities (temperature: 20 °C); b) at different temperatures (flow velocity: 6.9 cm/s) for $Na_2SO_4$ (0.01 M/0.30 M) solution.

A change in temperature has only a slight effect on OCV (Daniilidis et al., 2014b; Tufa et al., 2015). As shown in Figure 4b, the OCV increased by 4% (from 11.8 V to 12.3 V) when raising the temperature of the $Na_2SO_4$ solutions from 15 to 35°C. This is in agreement with expectations since, from a thermodynamic point of view, OCV increases with temperature (Eq. S1 in the Supporting Information). However, this effect is restricted by parasitic current.

### *3.2.2. Internal stack resistance*

Internal stack resistance predominantly corresponds to the Ohmic resistance of the feeds and membranes (Avci et al., 2016; Fontananova et al., 2017; Fontananova et al., 2014; Veerman et al., 2008; Vermaas et al., 2011). For large stacks with a high number of membranes and cell pairs, Ohmic losses over electrodes and electrode polarization losses can be neglected (Veerman et al., 2008; Veerman et al., 2010b).

Figure 5a presents the dependence of internal area resistance per cell (IAR) on flow velocity and temperature. By increasing the flow velocity from 0.6 m/s to 6.9 m/s, the IAR dropped by about 26% from 94 to 70 $\Omega cm^2$/cell. The decrease in IAR at high flow velocity can be ascribed to enhanced mixing of the feed solutions which results in the transport of ions from the HCC to the LCC, thereby limiting the influence of the resistance of the LCC (Długołęcki et al., 2010a; Długołęcki et al., 2010b). In addition, boundary layer resistance also decreases significantly [Not the general rule, but for emphasis] at high flow velocities due to a reduction in thickness of the diffusion boundary layer (Vermaas et al., 2011). A previous study of a lab-scale RED stack (25

cells) led to a 0.14 Ω cm$^2$ reduction in IAR per 0.1 cm/s increase in fluid velocity (Tufa et al., 2015). Długołecki *et al*. observed a significant reduction in internal stack resistance of a RED (3 cells) when operated at a flow velocity above 0.3 cm/s (Długołęcki et al., 2009).

The IAR decreases monotonically with rising temperature. A significant reduction in IAR of up to 45 % from 78.8 to 43.2 Ωcm$^2$/cell was recorded when the temperature of the feed solutions was increased from 15 $^o$C to 35 $^o$C. Raising feed temperature increases ionic conductivity, enhances ionic mobilities and, ultimately, reduces stack resistance. Considering that Ohmic resistances largely predominate, an almost linear trend between IAR and temperature can be assumed, and a reduction of 1.8 Ωcm$^2$/cell/$^o$C is computed within the experimental temperature range.

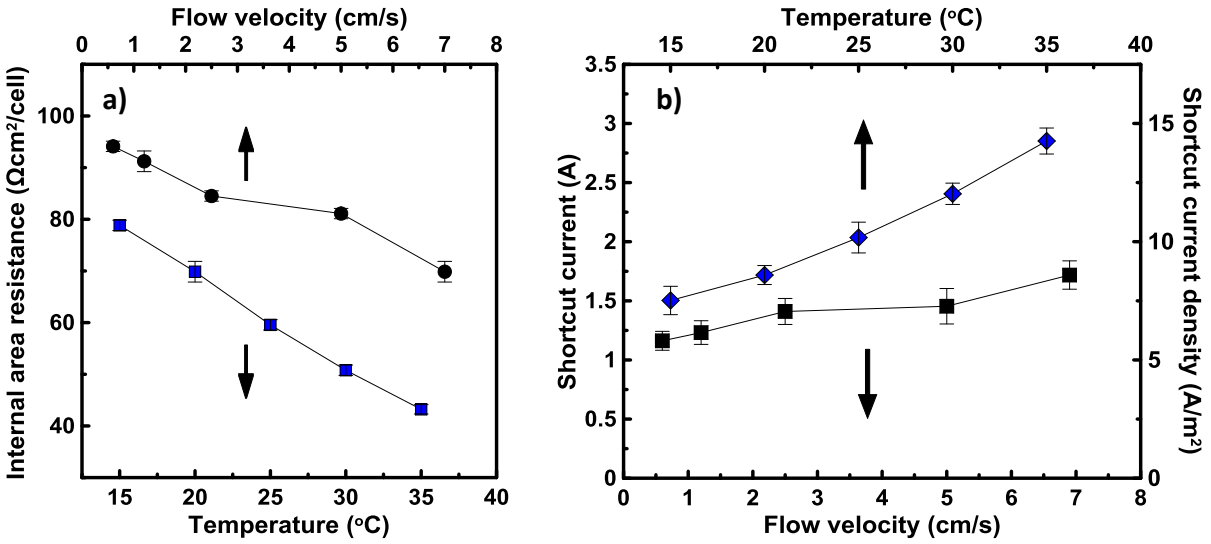


**Figure 5.** The variation of a) IAR b) ionic shortcut currents with temperature (flow velocity: 6.9 cm/s) and flow velocity 6.9 cm/s (temperature: 20 $^o$C) for $Na_2SO_4$ (0.01 M/0.30 M) solution.

Figure 5b presents the variation in $I_s$ with flow velocity and temperature. In fact, $I_s$ depends on both OCV and $R_i$ (Eq. S4 in the Supporting Information). $I_s$ also depends on operating conditions: it increases with an increase in flow velocity, which is associated with an increase in conductivity of the LCC solution due to enhanced mixing. Since the OCV is hardly influenced by temperature, the change in $I_s$ can be correlated to the change in $R_i$, which is assumed to be a linear function of temperature. On average, $I_s$ increases with a rise in temperature at a rate of 0.1 A/$^o$C. The $I_s$ of the present pilot-scale RED stack was comparatively higher than that of our previous investigation of a

small-scale RED stack (25 cells) which indicated an average increment rate of about 0.02 A/°C (Tufa et al., 2015; Tufa et al., 2014). Although the difference in stack design and operating conditions precludes a direct comparison, the general observation is that $I_s$ increases when the RED stack is scaled up (Tedesco, Michele et al., 2015).

*3.2.3. Power density*

Figure 6 shows the dependence of power density on feed flow velocity and temperature. The power density progressively increases with flow velocity within the experimental range. $P_{d,max}$ increased by about 66% from 0.08 to 0.13 W/m$^2$MP (Figure 6a) when the flow velocity was increased from 0.6 to 6.9 cm/s. High flow velocities result in low residence time of feed in the stack, which consequently leads to a higher average salinity gradient between the compartments and, ultimately, to improved driving force (Tedesco, M et al., 2015). However, conversely, excessively high feed velocity and hence very low residence time may increase the stack resistance due to the low conductivity of the solution in the LCC (Tedesco, M et al., 2015; Tedesco et al., 2012). This also gives rise to a reduction in energy efficiency of the RED (Veerman et al., 2009, 2010a, 2011; Vermaas et al., 2013). Moreover, it is worth noting that higher flow velocities result in an increase in pressure drop and pumping energy requirements.

$P_{d,max}$ doubled from 0.11 W/m$^2$MP to 0.22 W/m$^2$MP when the temperature of the feed solutions was increased from 15 to 35°C (Figure 6b). A linear trend of $P_{d,max}$ as a function of temperature with a slope of 5.7 mW/m$^2$MP/°C was observed. Temperature has a direct impact on the increase in thermodynamic driving force, ionic mobility and feed conductivities and on the decrease in membrane resistance. This leads to an overall reduction in Ohmic losses, thereby enhancing the power density. Danilidis *et al.* observed an increase of up to 50 % in $P_{d,max}$ (from 7.6 to 13.4 W/m$^2$MP) on heating up the feed solution (0.01 M/5 M NaCl) from 25°C to 60°C, corresponding to a rate of change of ~167 mW/m$^2$MP/°C (Daniilidis et al., 2014b). For RED tests with artificial brine (5 M NaCl) and seawater (0.5 M NaCl), a 44% increase in $P_{d,max}$ was reported on raising the feed temperature from 10 to 50°C, corresponding to a rate of change of ~27 mW/m$^2$MP/°C (Tufa et al., 2015). Moreover, Tedesco *et al*. reported a $P_{d,max}$ increase in the range of 40-50% (up to 6 W/m$^2$MP) accompanied by a 30-50% reduction in internal stack resistance on increasing the feed (artificial brackish water/brine: 0.1 M/5 M NaCl) temperature from 20 to 40 °C, corresponding to a rate of change of ~175 mW/m$^2$MP/°C

(Tedesco, M et al., 2015). A recent study shows a 25% increase in power density for RED when heating up the feed stream (artificial river water/seawater: 0.017 M/0.5 M NaCl) from 20 °C to 40 °C, corresponding to a rate of change of ~20 mW/m$^2$MP/$^o$C (Benneker et al., 2017). In general, the increase in $P_{d,max}$ with the rise in feed temperature assures the advantage of the thermal heat contained in wastewater.

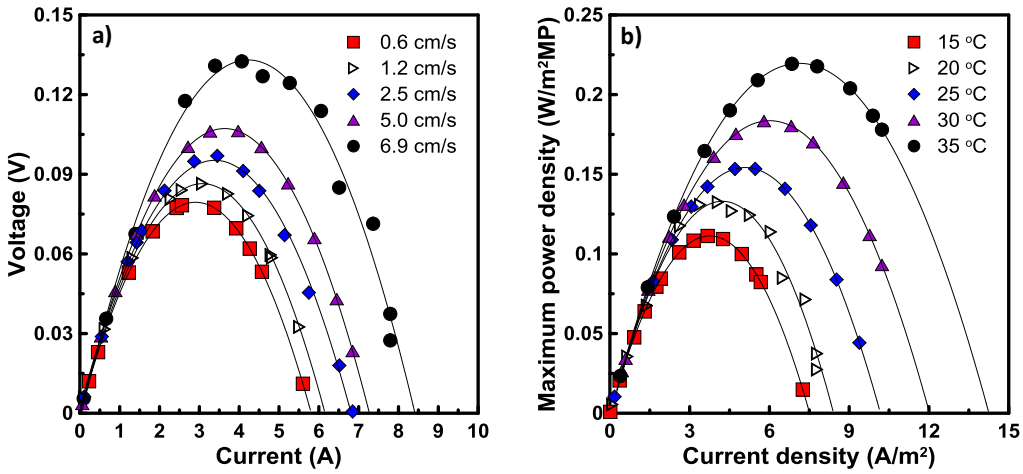


**Figure 6.** Power curves at different flow velocities (temperature: 20 $^o$C) and b) temperatures (flow velocity: 6.9 cm/s) for $Na_2SO_4$ (0.01 M/0.3 M) feed solutions.

It is worth noting that an increase in both feed temperature and flow velocity boosts the energy consumption; this requires an appropriate techno-economic analysis to establish the optimal operating conditions (Gurreri et al., 2012; Tufa et al., 2015). With regard to temperature, the availability of low-grade waste heat makes it beneficial, irrespective of the cost of the input energy (Forman et al., 2016; Luo et al., 2012; Tufa et al., 2017). This represents a huge advantage in terms of synergetic conversion of the electrochemical potential of waste streams and low-grade waste heat into electricity, and further storage as hydrogen by coupling RED with APWEL.

### *3.3. Hydrogen production by alkaline water electrolysis*

The use of non-intermittent RED power to fuel APWEL enables clean and sustainable hydrogen production. The performance of an APWEL system depends on several operating parameters, such as temperature, liquid electrolyte concentration, catalyst and binder loadings (Tufa et al., 2016; Zeng, K. and Zhang, D., 2010).

340 *3.3.1. Influence of temperature.*

341 Temperature influences the Ohmic loss and kinetics of an electrochemical reaction
342 at the three-phase interface (electrode, catalyst and electrolyte) (Kang et al., 2017; Lee
343 et al., 2016). In this regard, an increase in temperature is expected to reduce the stack
344 voltage needed to attain the required current density (Li et al., 2016; Marini et al., 2012).
345 A rise in temperature improves the performance of a water electrolysis system to a
346 certain extent (Figure 7a): when the temperature is raised from 28 to 48°C the stack
347 voltage progressively decreases from 11.2 V to 10.6 V. A current density of 75 mA/cm$^2$
348 was recorded at 28°C and cell voltage of 1.85 V. When raising the electrolyte
349 temperature to 48°C, the current density increased to 110 mA/cm$^2$. A voltage of 1.85 V
350 was chosen as the value corresponding to the lower limit of industrial operational
351 conditions which is equivalent to a thermoneutral efficiency of 80 % vs. $V_{th}$ of water
352 splitting (see Section 2.2.1).

353 The impact of temperature, particularly on the overpotential of the oxygen
354 evolution reaction at the anode which is detrimental to the overall cell performance, is
355 significant (Xu et al., 2011; Zhang et al., 2006). A study of micro-alkaline water
356 electrolyzers by Wendt *et al*. indicated a 20% reduction (from 0.35 V to 0.28 V) of
357 oxygen overpotential by shifting the temperature from 90 to 160°C at a current density
358 of 1 A/cm$^2$ (Wendt and Plzak, 1983).

359 *3.3.2. Influence of electrolyte concentration.*

360 Figure 7b shows the effect of electrolyte concentration on the performance of the
361 APWEL stack. The cell voltage declines moderately with an increase in electrolyte
362 (KOH) concentration. For a current density in the range of 90-390 mA/cm$^2$, the cell
363 voltage drops, on average, by 2.5% on increasing the KOH concentration from 0.85 M
364 to 2.5 M at 48°C. At a cell voltage of 1.85V and 48°C, corresponding to $V_{\text{stack}}$ of 11.1 V,
365 the current density increases from 86 to 110 mA/cm$^2$ when the KOH concentration is
366 shifted from 0.85 M to 2.5 M KOH. The use of concentrated KOH improves the
367 conductivity of the electrolyte, thus facilitating the ionic contact between the catalytic
368 layer and the membrane, and it improves utilization of the 3D structure of the electrode,
369 thereby enhancing the electrolyzer's performance. A recent study by Hnát *et al*. on a
370 single-cell alkaline electrolyzer equipped with a novel 1,4-diazabicyclo[2.2.2]octane
371 (DABCO)-functionalized AEM indicated an approximately 20% increase in current

density (i.e. from ~25 mA/cm$^2$ to 31 mA/cm$^2$) when the concentration of KOH electrolyte was increased from 0.18 M to 2.7 M at 1.8 V and 40 °C (Hnat et al., 2017). A maximum current density of 150 mA/cm$^2$ was reported under operating conditions of 2.7 M KOH, 2 V and 40 °C. This was comparable to that of commercial electrolyzers with a current density ranging from 100 to 300 mA/cm$^2$ at 5 M KOH (ionic conductivity of 1.5 S/cm at 80 °C) and 1.8-2 V (Varcoe et al., 2014).

On the other hand, at a higher concentration of KOH electrolyte, the increase in viscosity complicates the recirculation of electrolyte, especially at low temperatures. In a bipolar stack configuration, a higher concentration of circulating electrolyte will increase the conductivity of distribution channels, however at the cost of increased parasitic currents. The stability of the MEA under the aggressive environment of highly concentrated KOH solutions remains a challenge (Hnat et al., 2017).

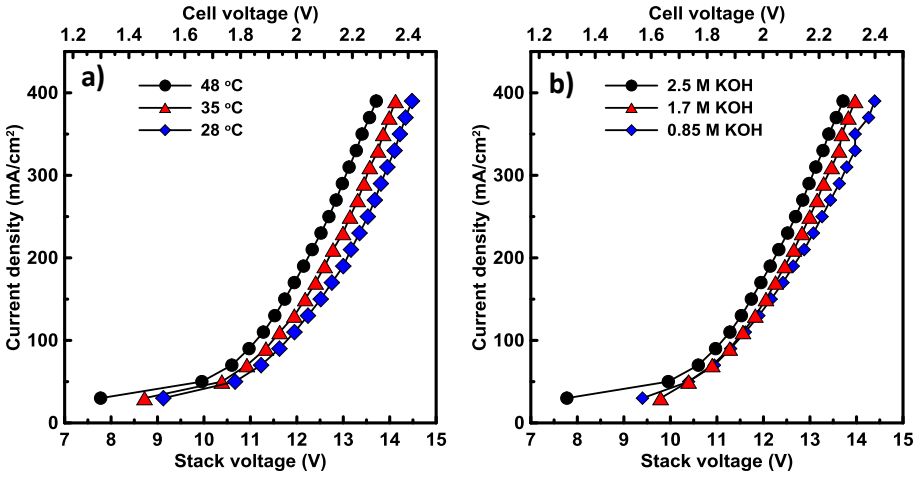


**Figure 7.** Influence of: a) temperature (liquid electrolyte: 2.5 M KOH); b) electrolyte (KOH) concentration (temperature: 48°C) on the current density of the APWEL stack (6 cells). Separator: heterogeneous ASM; electrodes: Ni foam (surface area 25 cm$^2$); electrolyte flow rate: 340 ml/min.

*3.3.3. Hydrogen production rate*

Figure 9a shows hydrogen production rate (HPR) data at varying KOH concentrations, temperatures and current efficiencies. Details on current efficiency determination are provided in the Supporting Information. At 1.85V and 48°C, the current density of the APWEL stack varies in the range of 88-110 mA/cm$^2$ for KOH concentrations in the range of 1.7-2.5 M. The results indicate a moderate increase in HPR with an increase in both temperature and KOH concentration. The HPR,

normalized to an electrode area of 25 $cm^2$, increased from 40 to 50 $cm^3/h \cdot cm^2$ ($1.6\times10^{-3}$ to $2.0\times10^{-3}$ $mol/h \cdot cm^2$) when the KOH concentration was changed from 0.85 to 2.5 M at 48 °C. Under optimal conditions, when the maximum HPR reached 50 $cm^3/h \cdot cm^2$, the electrolyzer energy consumption was about 5 $kWh/Nm^3$ of $H_2$. A previous study of a single-cell APWEL stack indicated a current density of 57 $mA/cm^2$, corresponding to a HPR of 26 $cm^3/h \cdot cm^2$ ($1.1\times10^{-3}$ $mol/h \cdot cm^2$) at a cell voltage of 1.85 V, 1.7 M KOH electrolyte solution and 45 $^oC$ (Tufa et al., 2016). This is comparable to the present APWEL stack which attained a HPR of 45 $cm^3/h \cdot cm^2$ ($1.8\times10^{-3}$ $mol/h \cdot cm^2$) under similar conditions.

In order to identify the operating point where the power requirement of the APWEL meets the power output of the RED stack, the polarization curves of the two systems were analyzed concurrently. Figure 9b presents the polarization curves of the APWEL stack and the pilot-scale RED stack. Under optimal conditions (1.85 V, 2.5 M KOH), the current flow in the APWEL stack is 2.75 A and the $V_{stack}$ is 11.1 V. This corresponds to a total power dissipation of 30.3 W. In order to achieve this power dissipation, the number of cells in the SGP-RED stack was increased to 373 cells for operations with $Na_2SO_4$ (0.01 M/0.3 M at 35$^oC$). Under these conditions, the polarization curve of the RED stack and APWEL stack intersect at a cell voltage of 1.85 V and a current of 2.75 A, attaining a HPR of 50 $cm^3/h \cdot cm^2$.

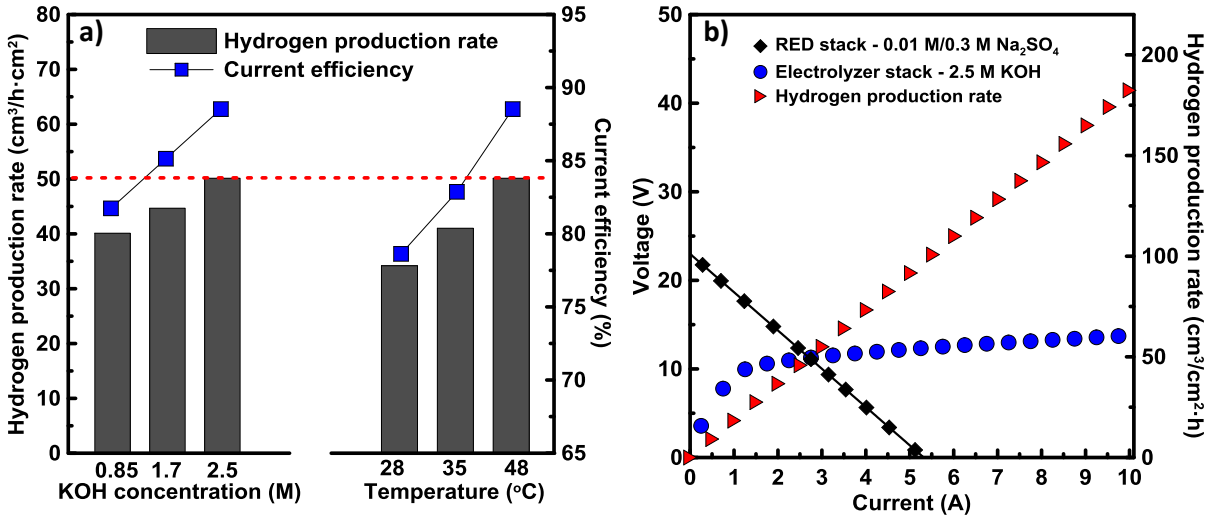


421

422 **Figure 9** a) The variation of HPR with concentration of KOH (0.8 - 2.5 M) and
423 temperature (28-48°C) at different current density (88 - 110 mA/cm$^2$) and current
424 efficiency (81-89 %) values; b) Current-voltage curves of the SGP-RED stack and the
425 APWEL stack: the curves intersect at a stack current of 2.75 A and stack voltage of 11.1
426 V, corresponding to power of 30.3 W. RED conditions: 373 cells and 35 °C. Electrolyzer
427 conditions: 2.5 M KOH and 48°C.

428 The values of the HPR achieved in the present study can be compared with those
429 in other studies focused on RED-assisted electrolyzers of different designs. Kim and
430 Logan combined reverse electrodialysis (5 cells) and microbial electrolysis cells
431 (electrode chamber volume: 30 mL, cathode projected area: 7 cm$^2$) for hydrogen
432 production from organic matter (Kim and Logan, 2011). This system, indicated as
433 MREC and operated with salinity gradient energy produced by mixing river water and
434 seawater, attained a HPR of 0.8-1.6 m$^3$H$_2$/m$^3$/d (0.6-1.3×10$^{-5}$ mol H$_2$/h·cm$^2$) (Kim and
435 Logan, 2011). Nam *et al*. reported a maximum hydrogen production rate of 1.6
436 m$^3$H$_2$/m$^3$/d (1.3×10$^{-5}$ mol H$_2$/h·cm$^2$) using MREC (5 cells, electrode chamber volume:
437 30 mL and cathode projected area: 7 cm$^2$) driven by SGP produced from thermolytic
438 solutions of ammonium bicarbonate (Nam et al., 2012). Hatzell *et al*. attained a
439 hydrogen production rate of 8.7 ± 0.1 m$^3$ H$_2$/m$^3$/d (6.3×10$^{-6}$ mol H$_2$/h·cm$^2$) on the
440 cathode compartment of the RED unit (volume of the electrolyte rinse solutions: 80 mL
441 and cathode projected area: 207 cm$^2$) using a synthetic waste acid stream as the catholyte
442 (pH ≈ 2) (Hatzell et al., 2014). Notably, the hybrid system proposed in the present study,
443 exhibiting a HPR of up to 2.0 x10$^{-3}$ mol/h·cm$^2$, significantly outperforms the
444 aforementioned studies on standalone and/or integrated application of RED for
445 hydrogen production.

Although technically possible, single-step hydrogen production directly on RED electrodes is very demanding from the point of view of design and operation: the electrolyzer would require a sufficient number of RED cells in order to provide the necessary voltage at the terminal electrodes, each stack corresponding to just a single alkaline water electrolysis cell. Each such cell needs to be equipped with the necessary hydraulic and gas separation infrastructure. As a result, the complexity of the entire system would increase enormously. On the other hand, integrating RED with a separate APWEL unit offers the advantage of flexibility, with the possibility to use the excess power produced by RED exclusively for grid power supply or simultaneously with hydrogen production.

## 5. Economic aspects

The cost of the hybrid RED-APWEL system proposed in the present study operating on industrial sulfate waste streams calls for a breakdown of the individual units. The cost of electricity from industrial waste streams is directly related to that of installing a RED plant. The cost of a RED plant is mainly dependent on the membranes. In fact, given a current membrane price of about 50 €/$m^2$, RED is a more expensive technology than other renewable energy sources like wind and solar (Daniilidis et al., 2014a). However, with process intensification the use of novel, low-cost membranes would make a huge contribution to the reduction of the cost of RED in the near future. A feasibility study shows that the cost of electricity could drop to 0.18 €/kWh, given that cheap raw materials and manufacturing technologies could reduce the membrane price to 4.3 €/$m^2$ (Daniilidis et al., 2014a). Moreover, further optimization of RED would result in levelized costs of electricity of about 0.11-0.20 €/kWh by 2020. The critical issue concerning the use of $SO_4^{2-}$-rich waste streams in RED is system performance, which requires further optimization.

The cost perspective for alkaline water electrolysis is quite different from that of RED. A typical electrolyzer set-up consists of an electrolysis stack and storage units based on a conventional cylinder tank or tailored ones with a specific material that adsorbs and desorbs hydrogen. All of these factors contribute to the total installation cost which depends mainly on plant size and site- specific characteristics. For a capacity in the range of 1,000- 1,200 €/kW, Bertuccioli *et al*. estimated 1,100 €/kW as the main investment cost with a projected large potential decrease to 580 €/kW by 2030 (Luca Bertuccioli, 2014).

A system cost breakdown for alkaline water electrolysis reveals that the stack accounts for up to 50% of the overall cost. Membranes contribute only about 7% of the overall stack cost and about 3.5% of the entire system (Kuckshinrichs et al., 2017). Therefore, the impact of introducing a new membrane is not a major issue in terms of the overall cost of alkaline water electrolysis systems unlike the case of RED.

## 4. Conclusions and outlook

The use of $SO_4^{2-}$-rich industrial waste streams for power generation represents a promising alternative for the valorization of industrial waste streams. An APWEL stack, continuously fuelled by SGP-RED operating on industrial waste streams, ensures an environmentally benign hydrogen production route. A maximum HPR of 50 $cm^3/h \cdot cm^2$ was attained under the best conditions (1.85 V/cell, 2.5 M KOH, 48°C). However, further optimization in terms of materials and process is required to meet commercial requirements. The use of highly active, stable electrodes and electrocatalysts both for the anodic and cathodic reactions along with the development of a highly conductive and stable ASM are among the core research targets to improve the efficiency of APWEL. Moreover, an improved design of the APWEL stacks would also facilitate efficient pressurization; this would bring about a huge cost reduction and plant simplification, without the need for subsequent hydrogen compression. For RED, further optimization of ion-exchange membranes for fast transport of $SO_4^{2-}$ ions is crucial to enhance the output power of RED. The apparent permselectivity of membranes in $Na_2SO_4$ is low due to lower ionic flux ($5.58 \times 10^{-8}$ $mol/cm^2 \cdot s$) and low bulk transport number (0.449) of $SO_4^{2-}$ ions across AEMs (Güler et al., 2014). Future research should also focus on optimal stack design, reduction of hydraulic friction losses, assessment of pre-treatment requirements and exploration of various other wastewater resources for power generation (Act, 2003; Di Salvo et al., 2017; Dil et al., 2018; Dil et al., 2016; Siles et al., 2010). Moreover, a more advanced techno-economic assessment of the RED-APWEL system using industrial waste streams with different operating conditions, system design and efficiency and supported by experimental outputs, is the subject of future studies.

## Acknowledgments

The financial support of the Education, Audiovisual and Culture Executive Agency (EACEA) under the Program "Erasmus Mundus Doctorate in Membrane Engineering"-EUDIME (FPA 2011-0014) is kindly acknowledged. Ramato A. Tufa acknowledges the financial support of the European Union's Horizon 2020 research and innovation programme under the Marie Skłodowska-Curie Actions IF Grant agreement No. 748683. Additionally, the financial support of this research received from the Grant Agency of the Czech Republic under project No. 16-20728S is gratefully acknowledged.

## References

Act, T., 2003. Standards for Effluent Discharge Regulations. Ministry of Environment and Sustainable Development: Port Louis, Port Louis District, Mauritius.

Avci, A.H., Sarkar, P., Tufa, R.A., Messana, D., Argurio, P., Fontananova, E., Di Profio, G., Curcio, E., 2016. Effect of $Mg^{2+}$ ions on energy generation by Reverse Electrodialysis. Journal of Membrane Science 520, 499-506.

Benneker, A.M., Rijnaarts, T., Lammertink, R.G.H., Wood, J.A., 2018. Effect of temperature gradients in (reverse) electrodialysis in the Ohmic regime. Journal of Membrane Science 548, 421-428.

Bobicki, E.R., Liu, Q., Xu, Z., Zeng, H., 2012. Carbon capture and storage using alkaline industrial wastes. Prog Energ Combust 38(2), 302-320.

Chanda, D., Hnat, J., Dobrota, A.S., Pasti, I.A., Paidar, M., Bouzek, K., 2015. The effect of surface modification by reduced graphene oxide on the electrocatalytic activity of nickel towards the hydrogen evolution reaction. Physical Chemistry Chemical Physics 17(40), 26864-26874.

Daniilidis, A., Herber, R., Vermaas, D.A., 2014a. Upscale potential and financial feasibility of a reverse electrodialysis power plant. Applied Energy 119, 257-265.

Daniilidis, A., Vermaas, D.A., Herber, R., Nijmeijer, K., 2014b. Experimentally obtainable energy from mixing river water, seawater or brines with reverse electrodialysis. Renewable Energy 64, 123-131.

Di Salvo, J.L., Cosenza, A., Cipollina, A., Tamburinia, A., Micale, G., 2017. Experimental analysis of a continuously operated reverse electrodialysis unit fed with wastewaters. Chemical Engineering Transactions 60, 307-312.

Dil, E.A., Ghaedi, M., Asfaram, A., Bazrafshan, A.A., 2018. Ultrasound wave assisted adsorption of congo red using gold-magnetic nanocomposite loaded on activated carbon: Optimization of process parameters. Ultrasonics Sonochemistry 46, 99-105.

Dil, E.A., Ghaedi, M., Asfaram, A., Mehrabi, F., 2017a. Application of modificated magnetic nanomaterial for optimization of ultrasound-enhanced removal of $Pb^{2+}$ ions from aqueous solution under experimental design: Investigation of kinetic and isotherm. Ultrasonics Sonochemistry 36, 409-419.

Dil, E.A., Ghaedi, M., Ghezelbash, G.R., Asfaram, A., 2017b. Multi-responses optimization of simultaneous biosorption of cationic dyes by live yeast Yarrowia lipolytica 70562 from

551 binary solution: Application of first order derivative spectrophotometry. Ecotoxicology
552 and Environmental Safety 139, 158-164.
553 Dil, E.A., Ghaedi, M., Ghezelbash, G.R., Asfaram, A., Ghaedi, A.M., Mehrabi, F., 2016.
554 Modeling and optimization of $Hg^{2+}$ ion biosorption by live yeast Yarrowia lipolytica
555 70562 from aqueous solutions under artificial neural network-genetic algorithm and
556 response surface methodology: kinetic and equilibrium study. RSC Advances 6(59),
557 54149-54161.
558 Długołęcki, P., Anet, B., Metz, S.J., Nijmeijer, K., Wessling, M., 2010a. Transport
559 limitations in ion exchange membranes at low salt concentrations. Journal of Membrane
560 Science 346(1), 163-171.
561 Długołęcki, P., Gambier, A., Nijmeijer, K., Wessling, M., 2009. Practical potential of reverse
562 electrodialysis as process for sustainable energy generation. Environmental Science and
563 Technology 43(17), 6888-6894.
564 Długołęcki, P., Ogonowski, P., Metz, S.J., Saakes, M., Nijmeijer, K., Wessling, M., 2010b.
565 On the resistances of membrane, diffusion boundary layer and double layer in ion
566 exchange membrane transport. Journal of Membrane Science 349(1–2), 369-379.
567 Farrell, E., Hassan, M.I., Tufa, R.A., Tuomiranta, A., Avci, A.H., Politano, A., Curcio, E.,
568 Arafat, H.A., 2017. Reverse electrodialysis powered greenhouse concept for water- and
569 energy-self-sufficient agriculture. Applied Energy 187, 390-409.
570 Fontananova, E., Messana, D., Tufa, R.A., Nicotera, I., Kosma, V., Curcio, E., van Baak, W.,
571 Drioli, E., Di Profio, G., 2017. Effect of solution concentration and composition on the
572 electrochemical properties of ion exchange membranes for energy conversion. Journal of
573 Power Sources 340, 282-293.
574 Fontananova, E., Zhang, W., Nicotera, I., Simari, C., van Baak, W., Di Profio, G., Curcio, E.,
575 Drioli, E., 2014. Probing membrane and interface properties in concentrated electrolyte
576 solutions. Journal of Membrane Science 459(0), 177-189.
577 Forman, C., Muritala, I.K., Pardemann, R., Meyer, B., 2016. Estimating the global waste heat
578 potential. Renewable and Sustainable Energy Reviews 57(Supplement C), 1568-1579.
579 Götz, M., Lefebvre, J., Mörs, F., Koch, A.M., Graf, F., Bajohr, S., Reimert, R., Kolb, T.,
580 2016. Renewable Power-to-Gas: A technological and economic review. Renewable
581 Energy 85, 1371-1390.
582 Güler, E., Elizen, R., Saakes, M., Nijmeijer, K., 2014. Micro-structured membranes for
583 electricity generation by reverse electrodialysis. Journal of Membrane Science 458(0),
584 136-148.
585 Güler, E., Elizen, R., Vermaas, D.A., Saakes, M., Nijmeijer, K., 2013. Performance-
586 determining membrane properties in reverse electrodialysis. Journal of Membrane Science
587 446(0), 266-276.
588 Gurreri, L., Tamburini, A., Cipollina, A., Micale, G., 2012. CFD analysis of the fluid flow
589 behavior in a reverse electrodialysis stack. Desalination and Water Treatment 48(1-3),
590 390-403.
591 Hatzell, M.C., Zhu, X., Logan, B.E., 2014. Simultaneous Hydrogen Generation and Waste
592 Acid Neutralization in a Reverse Electrodialysis System. ACS Sustainable Chemistry &
593 Engineering 2(9), 2211-2216.
594 Hnát, J., Paidar, M., Schauer, J., Žitka, J., Bouzek, K., 2011. Polymer anion selective
595 membranes for electrolytic splitting of water. Part I: stability of ion-exchange groups and
596 impact of the polymer binder. Journal of Applied Electrochemistry 41(9), 1043-1052.
597 Hnát, J., Paidar, M., Schauer, J., Žitka, J., Bouzek, K., 2012. Polymer anion-selective
598 membranes for electrolytic splitting of water. Part II: Enhancement of ionic conductivity
599 and performance under conditions of alkaline water electrolysis. Journal of Applied
600 Electrochemistry 42(8), 545-554.

Hnat, J., Plevova, M., Zitka, J., Paidar, M., Bouzek, K., 2017. Anion-selective materials with 1,4-diazabicyclo[2.2.2]octane functional groups for advanced alkaline water electrolysis. Electrochimica Acta 248, 547-555.
Ju, W., Heinz, M.V.F., Pusterla, L., Hofer, M., Fumey, B., Castiglioni, R., Pagani, M., Battaglia, C., Vogt, U.F., 2018. Lab-Scale Alkaline Water Electrolyzer for Bridging Material Fundamentals with Realistic Operation. ACS Sustainable Chemistry & Engineering 6(4), 4829-4837.
Kang, Z., Mo, J., Yang, G., Li, Y., Talley, D.A., Retterer, S.T., Cullen, D.A., Toops, T.J., Brady, M.P., Bender, G., Pivovar, B.S., Green, J.B., Zhang, F.-Y., 2017. Thin film surface modifications of thin/tunable liquid/gas diffusion layers for high-efficiency proton exchange membrane electrolyzer cells. Applied Energy 206(Supplement C), 983-990.
Kim, Y., Logan, B.E., 2011. Hydrogen production from inexhaustible supplies of fresh and salt water using microbial reverse-electrodialysis electrolysis cells. Proceedings of the National Academy of Sciences of the United States of America 108(39), 16176-16181.
Lee, B.-S., Park, H.-Y., Choi, I., Cho, M.K., Kim, H.-J., Yoo, S.J., Henkensmeier, D., Kim, J.Y., Nam, S.W., Park, S., Lee, K.-Y., Jang, J.H., 2016. Polarization characteristics of a low catalyst loading PEM water electrolyzer operating at elevated temperature. Journal of Power Sources 309(Supplement C), 127-134.
Levene, J.I., Mann, M.K., Margolis, R.M., Milbrandt, A., 2007. An analysis of hydrogen production from renewable electricity sources. Solar Energy 81(6), 773-780.
Logan, B.E., Elimelech, M., 2012. Membrane-based processes for sustainable power generation using water. Nature 488(7411), 313-319.
Luca Bertuccioli, A.C., David Hart, Franz Lehner, Ben Madden, Eleanor Standen, 2014. Development of water electrolysis in the European Union. Cambridge, United Kingdon.
Luo, F., Wang, Y., Jiang, C., Wu, B., Feng, H., Xu, T., 2017. A power free electrodialysis (PFED) for desalination. Desalination 404, 138-146.
Luo, X., Cao, X., Mo, Y., Xiao, K., Zhang, X., Liang, P., Huang, X., 2012. Power generation by coupling reverse electrodialysis and ammonium bicarbonate: Implication for recovery of waste heat. Electrochem. Commun. 19, 25.
Mehrabi, F., Alipanahpour Dil, E., 2017. Investigate the ultrasound energy assisted adsorption mechanism of nickel(II) ions onto modified magnetic cobalt ferrite nanoparticles: Multivariate optimization. Ultrasonics Sonochemistry 37, 37-46.
Nam, J.-Y., Cusick, R.D., Kim, Y., Logan, B.E., 2012. Hydrogen Generation in Microbial Reverse-Electrodialysis Electrolysis Cells Using a Heat-Regenerated Salt Solution. Environmental Science & Technology 46(9), 5240-5246.
Quist-Jensen, C.A., Macedonio, F., Horbez, D., Drioli, E., 2017. Reclamation of sodium sulfate from industrial wastewater by using membrane distillation and membrane crystallization. Desalination 401, 112-119.
Siles, J.A., Brekelmans, J., Martín, M.A., Chica, A.F., Martín, A., 2010. Impact of ammonia and sulphate concentration on thermophilic anaerobic digestion. Bioresource Technology 101(23), 9040-9048.
Tedesco, M., Brauns, E., Cipollina, A., Micale, G., Modica, P., Russo, G., Helsen, J., 2015. Reverse Electrodialysis with saline waters and concentrated brines: a laboratory investigation towards technology scale-up. Journal of Membrane Science 492, 9-20.
Tedesco, M., Cipollina, A., Tamburini, A., van Baak, W., Micale, G., 2012. Modelling the Reverse ElectroDialysis process with seawater and concentrated brines. Desalination and Water Treatment 49(1-3), 404-424.
Tedesco, M., Mazzola, P., Tamburini, A., Micale, G., Bogle, I.D.L., Papapetrou, M., Cipollina, A., 2015. Analysis and simulation of scale-up potentials in reverse electrodialysis. Desalination and Water Treatment 55(12), 3391-3403.

Tedesco, M., Scalici, C., Vaccari, D., Cipollina, A., Tamburini, A., Micale, G., 2016. Performance of the first reverse electrodialysis pilot plant for power production from saline waters and concentrated brines. Journal of Membrane Science 500, 33-45.
Tufa, R.A., 2015. Perspectives on environmental ethics in sustainability of membrane based technologies for water and energy production. Environmental Technology & Innovation 4, 182-193.
Tufa, R.A., Chanda, D., Tundis, L., Hnát, J., Bouzek, K., Veerman, J., Fontananova, E., Di Profio, G., Curcio, E., 2017. Salinity gradient power driven water electrolysis for hydrogen production, Chemical Engineering Transactions. pp. 283-288.
Tufa, Ramato A., Curcio, E., Brauns, E., van Baak, W., Fontananova, E., Di Profio, G., 2015. Membrane Distillation and Reverse Electrodialysis for Near-Zero Liquid Discharge and low energy seawater desalination. Journal of Membrane Science 496, 325-333.
Tufa, R.A., Curcio, E., van Baak, W., Veerman, J., Grasman, S., Fontananova, E., Di Profio, G., 2014. Potential of brackish water and brine for energy generation by salinity gradient power-reverse electrodialysis (SGP-RE). RSC Advances 4(80), 42617-42623.
Tufa, R.A., Pawlowski, S., Veerman, J., Bouzek, K., Fontananova, E., di Profio, G., Velizarov, S., Goulão Crespo, J., Nijmeijer, K., Curcio, E., 2018. Progress and prospects in reverse electrodialysis for salinity gradient energy conversion and storage. Applied Energy 225, 290-331.
Tufa, R.A., Rugiero, E., Chanda, D., Hnàt, J., van Baak, W., Veerman, J., Fontananova, E., Di Profio, G., Drioli, E., Bouzek, K., Curcio, E., 2016. Salinity gradient power-reverse electrodialysis and alkaline polymer electrolyte water electrolysis for hydrogen production. Journal of Membrane Science 514, 155-164.
Varcoe, J.R., Atanassov, P., Dekel, D.R., Herring, A.M., Hickner, M.A., Kohl, P.A., Kucernak, A.R., Mustain, W.E., Nijmeijer, K., Scott, K., Xu, T., Zhuang, L., 2014. Anion-exchange membranes in electrochemical energy systems. Energy & Environmental Science 7(10), 3135-3191.
Veerman, J., Post, J.W., Saakes, M., Metz, S.J., Harmsen, G.J., 2008. Reducing power losses caused by ionic shortcut currents in reverse electrodialysis stacks by a validated model. Journal of Membrane Science 310(1-2), 418-430.
Veerman, J., Saakes, M., Metz, S.J., Harmsen, G.J., 2009. Reverse electrodialysis: Performance of a stack with 50 cells on the mixing of sea and river water. Journal of Membrane Science 327(1-2), 136-144.
Veerman, J., Saakes, M., Metz, S.J., Harmsen, G.J., 2010a. Electrical power from sea and river water by reverse electrodialysis: A first step from the laboratory to a real power plant. Environmental Science and Technology 44(23), 9207-9212.
Veerman, J., Saakes, M., Metz, S.J., Harmsen, G.J., 2010b. Reverse electrodialysis: evaluation of suitable electrode systems. Journal of Applied Electrochemistry 40(8), 1461-1474.
Veerman, J., Saakes, M., Metz, S.J., Harmsen, G.J., 2011. Reverse electrodialysis: A validated process model for design and optimization. Chemical Engineering Journal 166(1), 256-268.
Vermaas, D.A., Saakes, M., Nijmeijer, K., 2011. Doubled Power Density from Salinity Gradients at Reduced Intermembrane Distance. Environmental Science & Technology 45(16), 7089-7095.
Vermaas, D.A., Veerman, J., Yip, N.Y., Elimelech, M., Saakes, M., Nijmeijer, K., 2013. High Efficiency in Energy Generation from Salinity Gradients with Reverse Electrodialysis. ACS Sustainable Chemistry & Engineering 1(10), 1295-1302.

699 Wang, M., Wang, Z., Gong, X., Guo, Z., 2014. The intensification technologies to water
700 electrolysis for hydrogen production–A review. Renewable and Sustainable Energy
701 Reviews 29, 573-588.
702 Wendt, H., Plzak, V., 1983. Electrocatalytic and thermal activation of anodic oxygen- and
703 cathodic hydrogen-evolution in alkaline water electrolysis. Electrochimica Acta 28(1), 27-
704 34.
705 Xiao, L., Zhang, S., Pan, J., Yang, C., He, M., Zhuang, L., Lu, J., 2012. First implementation
706 of alkaline polymer electrolyte water electrolysis working only with pure water. Energy &
707 Environmental Science 5(7), 7869-7871.
708 Xu, W., Scott, K., Basu, S., 2011. Performance of a high temperature polymer electrolyte
709 membrane water electrolyser. Journal of Power Sources 196(21), 8918-8924.
710 Zeng, K., Zhang, D., 2010. Recent progress in alkaline water electrolysis for hydrogen
711 production and applications. Prog Energ Combust 36(3), 307-326.
712 Zeng, K., Zhang, D.K., 2010. Recent progress in alkaline water electrolysis for hydrogen
713 production and applications. Prog Energ Combust 36(3), 307-326.
714 Zhang, J., Xie, Z., Zhang, J., Tang, Y., Song, C., Navessin, T., Shi, Z., Song, D., Wang, H.,
715 Wilkinson, D.P., Liu, Z.-S., Holdcroft, S., 2006. High temperpature PEM fuel cells.
716 Journal of Power Sources 160(2), 872-891.

717
718